A New Forecasting Index for Solar Wind Velocity Based on EIT 284 Å Observations

**Bingxian Luo · Qiuzhen Zhong · Siqing Liu ·
Jiancun Gong**

Abstract Various solar wind forecasting methods have been developed during the past decade, such as the Wang – Sheeley model and the Hakamada – Akasofu – Fry Version 2 (HAFv2) model. Also, considerable correlation has been found between the solar wind speed v and the coronal hole (CH) area A_{M} on the visible side of the Sun, showing quantitative improvement of forecasting accuracy in low CME activity periods (*e.g.*, Vršnak, Temmer, and Veronig, *Solar Phys.* **240**, 315, 2007a). Properties of lower layers of the solar atmosphere are good indications of the subsequent interplanetary and geomagnetic activities. We analyze the SOHO/EIT 284 Å images and construct a new forecasting factor (Pch) from the brightness of the solar EUV emission, and a good correlation is found between the Pch factor and the 3-day-lag solar wind velocity (v) probed by the ACE spacecraft. The main difference between the Pch and A_{M} factor is that Pch does not depend on the CH-boundary estimate and can reflect both the area and brightness of CH. A simple method of forecasting the solar wind speed near Earth in low CME activity periods is presented. Between Pch and v from 21 November until 26 December 2003, the linear correlation coefficient is $R = 0.89$. For comparison we also analyze the data in the same period (DOY 25 – 125, 2005) as Vršnak, Temmer, and Veronig (*Solar Phys.* **240**, 315, 2007a), who used the CH areas A_{M} for predicting the solar wind parameters. In this period the correlation coefficient between Pch and v is $R = 0.70$, whereas for A_{M} and v the correlation coefficient is $R = 0.62$. The average relative difference between the calculated and the observed values is $\overline{|\delta|} \approx 12.15\%$. Furthermore, for the ten peaks during the analysis period, Pch and v show a correlation coefficient of $R = 0.78$, and the average relative difference between the calculated and the observed peak values is $\overline{|\delta|} \approx 5.83\%$. Moreover, the Pch factor can eliminate personal bias in the forecasting process, which existed in the method using CH area as input parameter, because CH area depends on the CH-boundary estimate but Pch does not. Until now the CH-boundary could not be easily determined since no quantitative criteria can be used to precisely locate CHs from observations, which led to differences in forecasting accuracy.

Keywords Sun: EUV emission · Sun: Solar wind

B. Luo (✉) · Q. Zhong · S. Liu · J. Gong
Center for Space Science and Applied Research, Chinese Academy of Sciences, Beijing 100190, China
e-mail: luobx@cssar.ac.cn

1. Introduction

Properties of lower layers of the solar atmosphere are good indications of subsequent interplanetary and geomagnetic activities. Recently, considerable attention has been paid to the Sun surface analysis by scientists (Persiantsev, Ryazanov, and Shugai, 2006). A number of spacecraft have been launched that now provide the possibility of obtaining high-quality images of the Sun in several spectral ranges (*e.g.*, the SOHO and the STEREO spacecraft, which carry EIT cameras; see Delaboudiniére *et al.*, 1995). Coronal holes (CHs), which are mainly observed in X-rays, extreme ultraviolet, and radio wavelengths (Kahler and Hudson, 2002), appear as dark regions (Bromage, Browning, and Clegg, 2001; Chertok *et al.*, 2001) in the SOHO EIT and STEREO EUVI images. Coronal holes are sources of fast solar wind (Gosling and Pizzo, 1999), predominantly associated with solar polar regions (Zhang *et al.*, 2002, 2003; McComas and Elliott, 2002). But, occasionally, CHs appear at low latitudes (Bromage, Browning, and Clegg, 2001), forming high-speed streams near Earth. The interaction of a fast stream and the upstream slow solar wind compresses the plasma and magnetic field at the boundary, causing density and magnetic enhancements in the upstream slow wind (Vršnak, Temmer, and Veronig, 2007a, 2007b). This solar wind feature is an important source of geomagnetic disturbances especially in the declining phase of the solar cycle (Watari, 1997; Borovsky and Denton, 2006). From a space weather aspect, fluctuations in the corotating interaction regions cause geomagnetic disturbances because of the southward interplanetary magnetic fields (IMFs) in the solar magnetospheric coordinate system (GSM) (Vršnak, Temmer, and Veronig, 2007a, 2007b). In addition, CHs are long-living formations with an average lifetime of several rotational periods of the Sun; thus the interaction region returns in each solar rotation. These recurrent corotating interaction regions (CIRs) cause recurrent geomagnetic disturbances (Bravo, 1996; Bravo, Cruz-Abeyro, and Rojas, 1998).

Recently, methods using CH area to forecast the solar wind velocity in periods of low CME activity have been developed by several scientists (Robbins, Henney, and Harvey, 2006; Veselovsky *et al.*, 2006; Vršnak, Temmer, and Veronig, 2007a, 2007b). Vršnak, Temmer, and Veronig (2007a) found that the daily average of solar wind speed is determined by the CH coverage in the M slice (meridional slice embracing the central meridian distance range [10°E, 10°W]). During their analysis interval (DOY 25 – 125 of 2005), the linear correlation coefficient between the CH areas A_{M} and the solar wind velocities v is $R = 0.62$ (Vršnak, Temmer, and Veronig, 2007a), for which the average relative difference between the calculated and the observed v of the eleven peaks is $\overline{|\delta|} \approx 10\%$. The other two papers showed similar results. Obviously, CH area depends on the CH boundary estimate. Unfortunately, until now no quantitative criteria were used to precisely locate CHs from observations (Zhao, Hoeksema, and Scherrer, 1999). The forecasting results of Vršnak, Temmer, and Veronig (2007a) are somewhat better than that of Robbins, Henney, and Harvey (2006). They explained that this might indicate that the determination of the CH areas by using SXI data offers better predictions than by using He I 1083-nm spectroheliograms. Obviously, personal bias existed in the methods of Vršnak, Temmer, and Veronig (2007a) and Robbins, Henney, and Harvey (2006). However, is there any other factor affecting the solar wind parameters near Earth? In the present analysis we consider not only the area but also the brightness of the CHs to construct a new forecasting factor to eliminate the personal bias and to improve forecasting accuracy.

2. The Data Set

We analyzed the daily solar images obtained in 1996–2006 with the Extreme ultraviolet Imaging Telescope (EIT) onboard the *Solar and Heliospheric Observatory* (SOHO) at a wavelength of 284 Å. The reason we employed the SOHO EIT 284 Å data to perform an analysis was that EIT provided complete observations of the corona in solar cycle 23. Furthermore, EIT 284 Å observes the corona at the greatest temperature and is almost as suitable for CH observations as soft X-ray emission (Shen *et al.*, 2006).

The solar wind data utilized in the present study were taken from the Solar Wind Electron, Proton, and Alpha Monitor (SWEPAM; McComas *et al.*, 1998) onboard the *Advanced Composition Explorer* (ACE; Stone *et al.*, 1998). Level-2 data of daily averages of the solar wind velocity v were used.
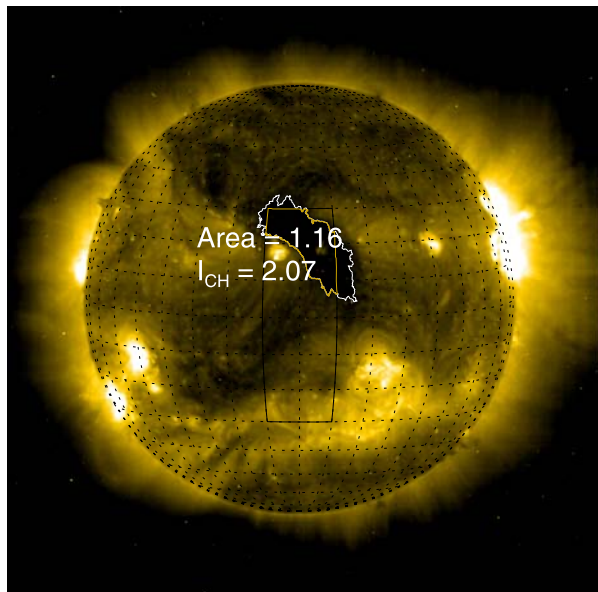
3. Analysis

3.1. Constructing a New Forecasting Index

As discussed in the first section, CHs are seen as dark regions on SOHO EIT images (Figure 1). Distinct correlations have been found between the daily averaged CH areas and the solar wind characteristics. The first step of our analysis here is to determine whether the brightnesses of the CHs have some relationship with the solar wind velocities. To examine how the brightness of EIT 284 Å images varied during solar cycle 23, we first calculated the intensity flux (F_{284}: the average of all the pixel values on the solar disk) of all the EIT 284 Å images from 1996 until 2006. F_{284} can be expressed as

$$F_{284} = \frac{\sum b}{N}, \tag{1}$$

Figure 1 Processed SOHO EIT 284 Å image containing the CH-area (% of solar hemisphere) averaged brightness (I_{CH}) of CH pixels inside the central equatorial region [10°E, 10°W], [30°N, 30°S].
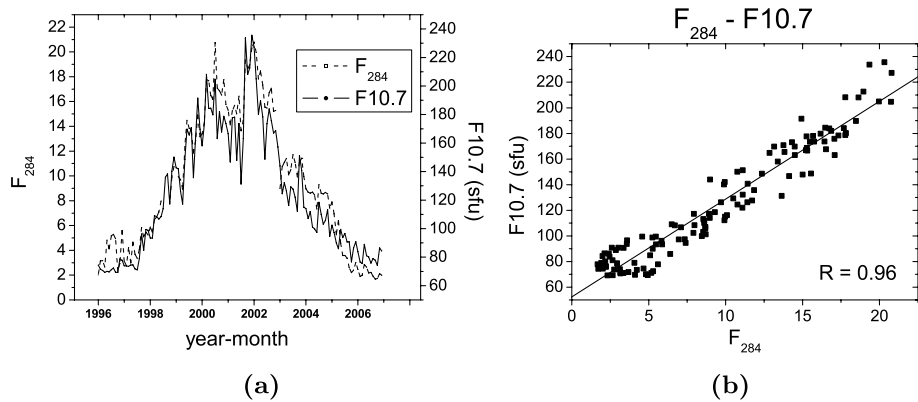
Figure 2 The monthly averaged EIT 284 Å and F10.7 flux intensity from 1996 to 2006. (a) Plots of EIT 284 Å and F10.7 intensity flux versus time. (b) Scatter plot of EIT 284 Å versus F10.7 intensity flux. The solid line represents linear least-squares fit to the data.

where b is the brightness (pixel value) of each pixel on the solar disk and N is the total number of these pixels. Then the monthly averaged F_{284} were calculated. The result is plotted in Figure 2(a). For comparison the monthly averaged F10.7 flux is overplotted. The linear correlation coefficient between these two fluxes is $R = 0.96$, as illustrated in Figure 2(b).

It can be seen from Figure 2 that F_{284} varied during solar cycle 23, which means that the brightness of SOHO images varied considerably. We examined dark regions (CHs) in the images and found that their brightness also varied during the solar cycle. Therefore, taking a fixed value or a fixed percentage of the brightness of the calibrated EIT 284 Å images for the CH areas as threshold does not seem to be appropriate, and a time-variable threshold for CH pixels should be applied. Here the brightness gradient method developed by Shen *et al.* (2006) is used. For an EIT 248 Å image, each pixel has its own recorded brightness b. For any given value of b, we can plot the contours and then calculate the area A enclosed by each contour. The derivative, $f = \delta b / \delta A$, is used to determine the boundaries of dark regions. The potential CH boundaries are at the places where $f = f_{\max}$. This is because the brightness usually increases rapidly at CH boundaries in the outward direction. For calculation of the CH area we applied the Lambert cylindrical equal-area projection to calculate the spherical surface area.

To investigate the interplanetary effect of the CH brightness, we collected all the equatorial CHs in 2002 and calculated the average brightness (I_{CH}) of all the pixels below the threshold (identified as CH pixels) inside the equatorial region ([10°E, 10°W], [30°N, 30°S]; Figure 1). I_{CH} is calculated as

$$I_{CH} = \frac{\sum b_{CH}}{N_{CH}}, \qquad (2)$$

where b_{CH} is the brightness (pixel value) of CH pixels inside the central equatorial region and N_{CH} is the total number of these CH pixels. We plotted this quantity versus the maximum hourly averaged solar wind velocities measured by the ACE spacecraft and fitted the scatter plot with a linear least-squares function (Figure 3(a)). We also examined the relationship between the longitudinal width (shown as Width) of the CHs and the corresponding geomagnetic disturbance duration (T_d; see Figure 3(b)). Here Width is the longitudinal width

Table 1 Equatorial CHs in 2002.

Data time[a] (UTC)	I_{CH}[b] $(DN\,s^{-1})$	v[c] (km/s)	Width[d] (°)	T_d[e] (hours)
03/02/2002	3.66	679	30	51
01/03/2002	2.78	702	40	75
23/03/2002	3.73	569	14	24
28/03/2002	2.42	788	45	108
24/04/2002	3.46	541	28	57
05/06/2002	3.97	497	45	87
02/07/2002	3.25	517	52	108
09/07/2002	2.41	542	15	30
16/07/2002	2.33	921	48	111
08/08/2002	2.49	515	52	45
07/09/2002	3.32	531	45	90
04/10/2002	2.50	512	50	117
16/10/2002	3.18	687	25	63
21/10/2002	2.56	766	80	201
31/10/2002	2.91	564	50	150
12/11/2002	2.99	486	30	27
27/11/2002	2.53	532	35	78
04/12/2002	3.49	641	28	66
15/12/2002	3.71	537	30	54
23/12/2002	1.84	760	45	96

[a]Day of the central meridian passage of the CH.

[b]Intensity of CH inside the central equatorial region ([10°E, 10°W], [30°N, 30°S]).

[c]Related maximum hourly averaged solar wind speed.

[d]Longitude width of CH between [30°N, 30°S].

[e]Related disturbance duration.

of CH regions between [30°N, 30°S]. The I_{CH}, v, Width, and T_d parameters are listed in Table 1.

The scatter plot of I_{CH} versus v in Figure 3(a) and its correlation coefficient of $R = 0.44$ indicate a weak correlation between these quantities. The linear least-squares fit to the Width versus T_d data, however, shows a much better correlation ($R = 0.87$; Figure 3(b)).

From this analysis we can see that the solar wind velocity is determined by not only the CH area but also the brightness. Larger and darker CHs in the equatorial region mostly produce higher solar wind velocities at 1 AU near Earth. We therefore try to construct another forecasting factor, Pch, that can reflect these two aspects. Here Pch, the sum of the reciprocal of all the pixel values (not only the CH pixels) inside the central equatorial region ([10°E, 10°W], [30°N, 30°S]), can be expressed as

$$Pch = \sum \frac{1}{b}, \tag{3}$$

where b is the brightness of the pixels inside the equatorial region ([10°E, 10°W], [30°N, 30°S]). From Figure 3(b) we can see that the choice of latitude range ([30°N, 30°S]) is reasonable.
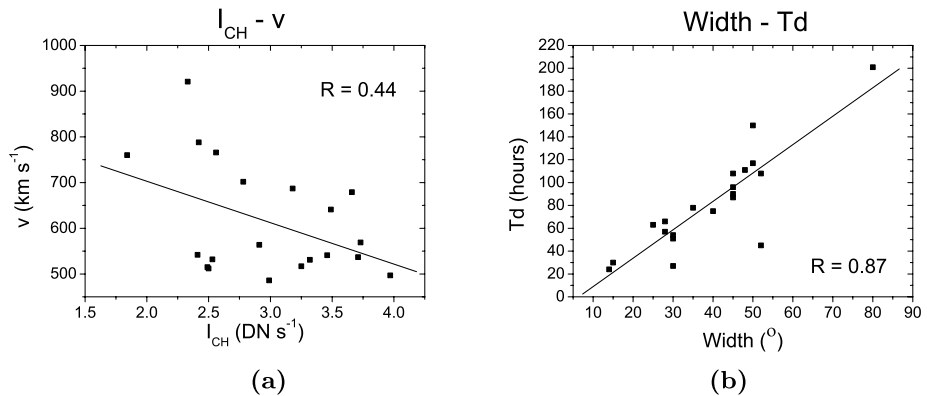
Figure 3 (a) Scatter plot of CH flux intensities I_{CH} versus the corresponding maximum hourly averaged solar wind velocities v during year 2002. (b) Scatter plot of CH widths Width versus related geomagnetic disturbance durations T_d. The solid lines represent linear least-squares fits to the data. The correlation coefficients of the fits (R) are indicated.

From this definition, we can see that the Pch factor does not depend on the CH-boundary estimate. Furthermore, in CHs, b values are small and have a large contribution to Pch, whereas pixels outside the CH regions have bigger b and contribute little. So, larger and darker CHs exhibit bigger Pch values, corresponding to higher solar wind velocities. Obviously, Pch can reflect both the area and brightness of CHs and can eliminate the personal bias in former forecasting methods using CH area, because in Pch there is no need to estimate the CH boundary.

In previous research the velocity peak was found to appear about 3.7 days after a low-latitude CH passes over the central meridian. For this reason, we may use Pch to predict the CH high-speed streams. Each day, four EIT 284 Å coronal images are provided around 1, 7, 13, and 19 UT. We used one EIT 284 Å coronal image per day taken around 1 UT to calculate the Pch factor. In the statistical analysis of Pch and solar wind speed, daily averaged ACE solar wind data were used.

3.2. Analysis of Pch and Corresponding ACE Solar Wind Speed

Obviously, a period of low CME activity is preferred. First we focus on a period of about one Carrington rotation during 2003, from 21 November until 26 December. During this period only two equatorial CHs existed. A faint halo CME occurred on DOY 337, so the data of this day are omitted. In Figure 4 we show plots for Pch, v, geomagnetic index Ap, and the cross-correlation functions for various combination of them. The time lags for the Pch$-v$, Pch$-$Ap, and $v-$Ap correlations are 3, 2, and -1 days, respectively. Figure 5 shows the relationships among Pch, the time-lagged solar wind speed v, and the geomagnetic index Ap. The linear least-squares fits and the corresponding correlation coefficients R are also provided in Figure 5. We can see that Pch and v show a very high correlation coefficient of $R = 0.89$, and v can be expressed as

$$v = 363 + 0.0126 \times \text{Pch}. \tag{4}$$

For Pch versus 2-day lagged geomagnetic index Ap the correlation coefficient is $R = 0.80$, while the correlation coefficient for v versus Ap is $R = 0.89$.
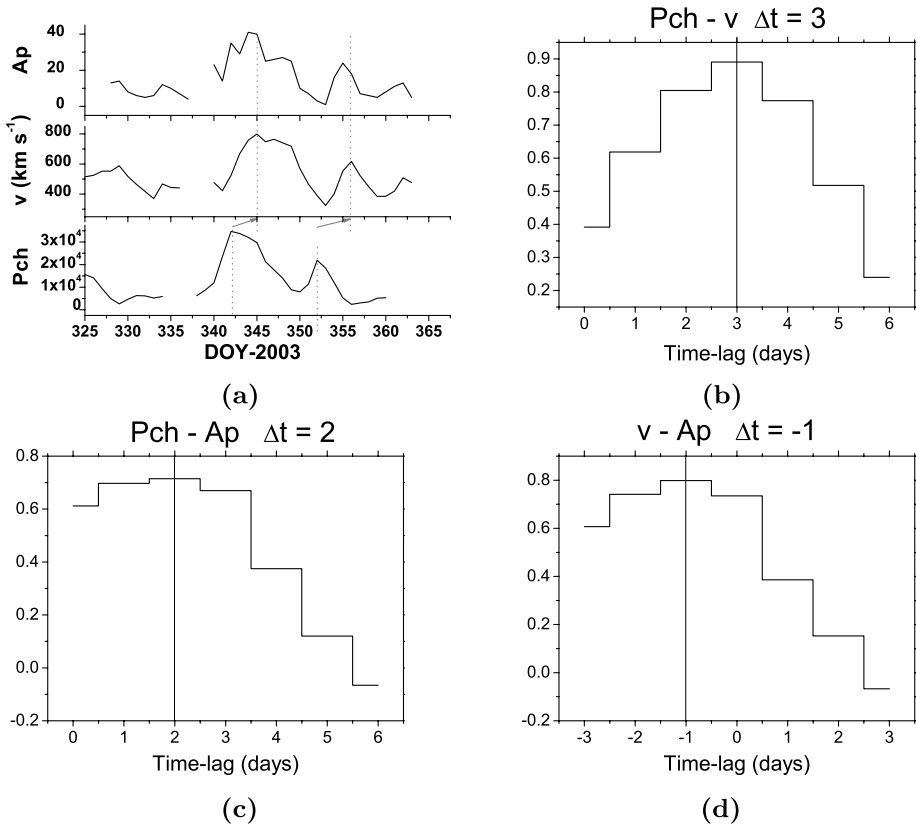
Figure 4 Plots of Pch, v, Ap, and cross-correlation coefficients derived from their various combinations.

From the previous analysis one can find that the solar wind speed can be predicted three days in advance by using the Pch parameter. Plots of the calculated and observed solar wind velocities are shown in Figure 6. The average relative difference between the calculated (C) and the observed (O) values [$\delta = (O - C)/C$] is $\overline{|\delta|} \approx 8.85\%$.

For comparison we also analyzed the data of the same period as Vršnak, Temmer, and Veronig (2007a), and the results are shown in Figure 7. The linear least-squares fits of Pch, the solar wind speed v, and the geomagnetic index Ap are plotted in Figure 8. Unfortunately, on some days there were no EIT images taken. We did not interpolate the missing Pch values. This left us with 81 days of data. The linear least-squares fit of Pch and the 3-day-lag solar wind velocities v can be expressed as

$$v = 337 + 0.00868 \times \text{Pch}. \tag{5}$$

With a high correlation coefficient of $R = 0.70$, the average relative difference between the calculated and the observed values is $\overline{|\delta|} \approx 12.15\%$.

Furthermore, for the ten peaks of our analysis, we present in Table 2 the DOY and the maximum value of Pch and the corresponding peak values of the solar wind speed v. The
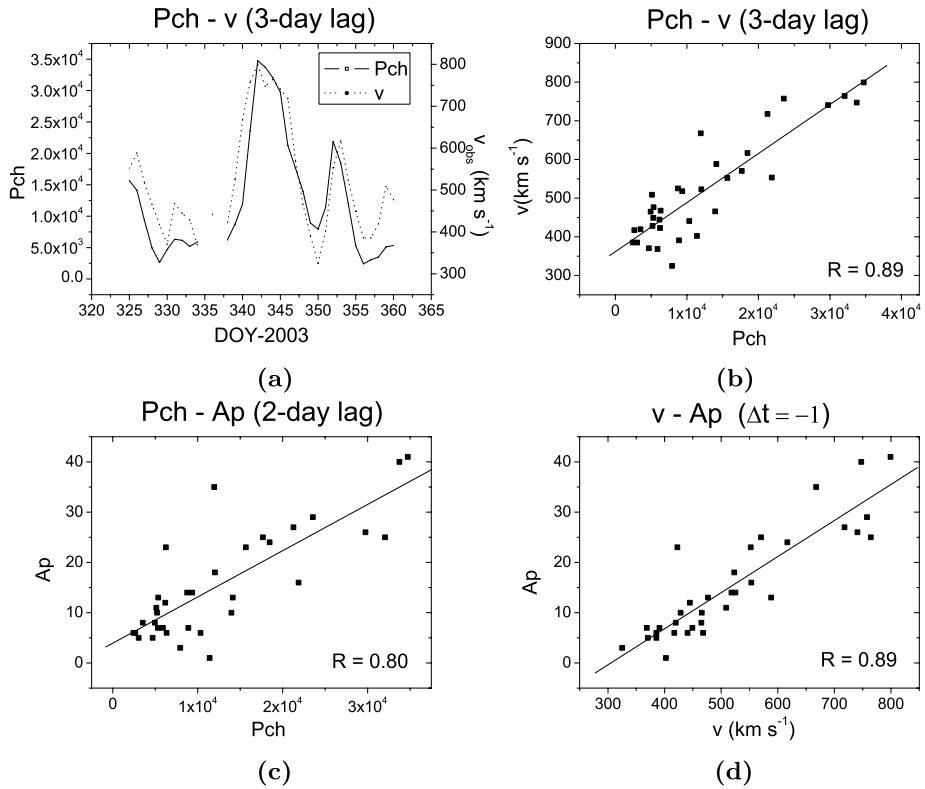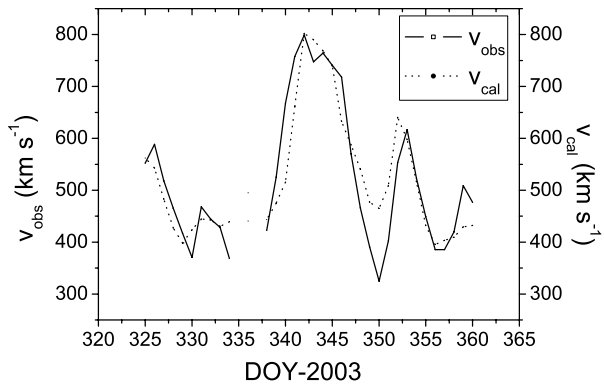
Figure 5 (a) Plots of Pch and the daily averaged solar wind velocities from 21 November until 26 December 2003. (b) Scatter plot of Pch versus the 3-day lagged solar wind speed v. (c) Scatter plot of Pch versus the 2-day lagged Ap. (d) Scatter plot of v versus Ap with a -1-day lag. The solid lines represent linear least-squares fits to the data. The correlation coefficients of the fits (R) are indicated.

Figure 6 Comparison of the calculated and the observed solar wind velocities from 21 November until 26 December 2003. The observed data are shown by a solid line; values calculated are shown by a dotted line.

linear correlation coefficient of Pch and v for the ten peaks is about $R = 0.78$ and can be expressed as

$$v = 443 + 0.00625 \times \text{Pch}. \qquad (6)$$

Figure 7 Plots of Pch, the daily averaged solar wind velocities v, and the geomagnetic index Ap from 25 January until 4 May 2005.
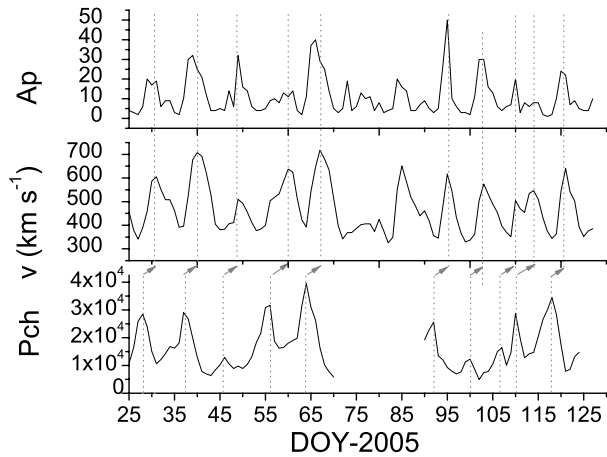

Table 2 For the twelve peaks during the time interval DOY 25 – 125, 2005, the fractional CH area measured in the M slice (A_{M}, where the M slice is the meridional slice embracing the central meridian distance range [10°E, 10°W]), the Pch factor, the corresponding peak values for the solar wind bulk speed v_{obs} as well as its delay Δt_v, and the calculated bulk speed v_{cal} using Equation (6) are given. In the sixth column, the relative difference between the calculated and the observed peak values are displayed. The standard deviations of these parameters are also listed in the last row of the table.

DOY 2005	A_{M}	Pch	v_{obs} (km s^{-1})	v_{cal} (km s^{-1})	δ(%)	Δt_v (days)
28	0.24	28446	605	620	2.63	3
37	0.18	29016	707	624	11.66	3
46	0.10	12868	509	522	2.74	3
57	0.34	31641	638	641	0.47	4
64	0.32	39500	717	690	3.70	3
73	0.09	–	406	–	–	–
82	0.37	–	651	–	–	–
92	0.32	25580	617	602	2.29	3
100	0.32	12270	574	519	9.55	3
107	–	16456	504	545	8.24	3
111	0.30	28716	546	622	14.03	4
118	0.36	34496	640	658	2.97	3
Average	0.27	25899	593	604	5.83	3.2
STD	0.10	9194	90	58	4.65	0.4

Compared with Equation (5) we can see that, for peak values, the slope of the linear least-squares fitting line is somewhat smaller, indicating that the solar wind speed increases as the CH in the central equatorial region grows larger and darker, but in smaller magnitude compared with the increase during the onset of a CH high-speed stream. The solar wind velocities for the ten peaks calculated by using Equation (6) are also listed in Table 2. The average relative difference between the calculated and the observed peak values is $\overline{|\delta|} \approx$ 5.83%. Furthermore, our procedure resulted in $\overline{|\delta|} < 15\%$ for all ten peaks. Also, in the second column of Table 2, maximum values of A_{M} from Vršnak, Temmer, and Veronig (2007a) for their eleven peaks are listed, and a linear least-squares analysis with the solar
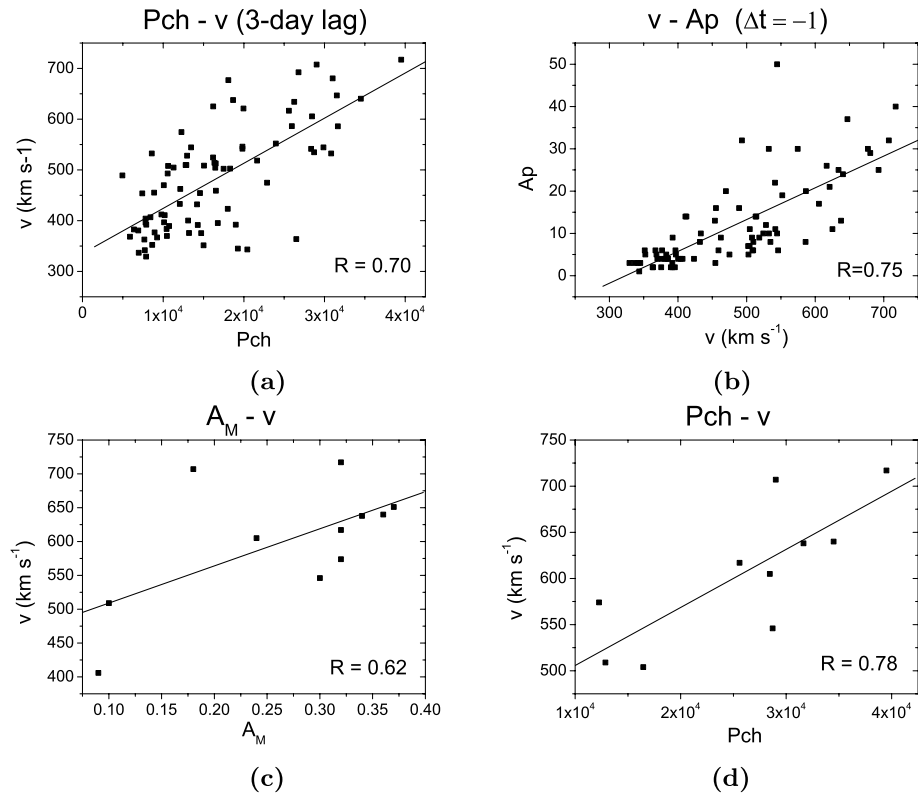
Figure 8 (a) Time-lagged correlation between Pch and solar wind velocity v during DOY 25 – 125, 2005. (b) Time-lagged correlation between Pch and Ap during DOY 25 – 125, 2005. (c) Time-lagged correlation between A_M and the corresponding solar wind velocities v for the eleven peaks. (d) Time-lagged correlation between Pch and the corresponding solar wind velocities v for the ten peaks. The solid lines represent linear least-squares fits to the data. The correlation coefficients of the fits (R) are indicated.

wind speed v is plotted, as shown in Figure 8. For the ten peaks for which Pch is available during the analysis period, Pch and v showed a correlation coefficient of $R = 0.78$, whereas for the eleven peaks, Pch and A_M showed about $R = 0.62$. A much larger data set would be required for the peak analysis comparison. On average, the velocity peak appeared 3.2 days after a low-latitude CH passed over the central meridian (*i.e.*, 3.2 days after Pch reached maximum; see the last column of Table 2). Considering that we used the EIT 284 Å images taken at about 1 UT every day, the real time lag was about 3.7 days. This is consistent with the result of Robbins, Henney, and Harvey (2006).

Finally, it should be emphasized that we repeated the whole procedure with no restriction in the latitudinal range (corresponding to latitude $\pm 90°$, shown as Pch$_{90}$). Inspecting Figure 9 one finds that Pch$_{90}$ shows linear correlation coefficients of about $R = 0.99$ and $R = 0.97$ with the former Pch values (shown as Pch$_{30}$), respectively, and their statistical significance with v do not increase. The result differs from the conclusion suggested by Vršnak, Temmer, and Veronig (2007a) that the latitude range restriction significantly degraded the correlations.
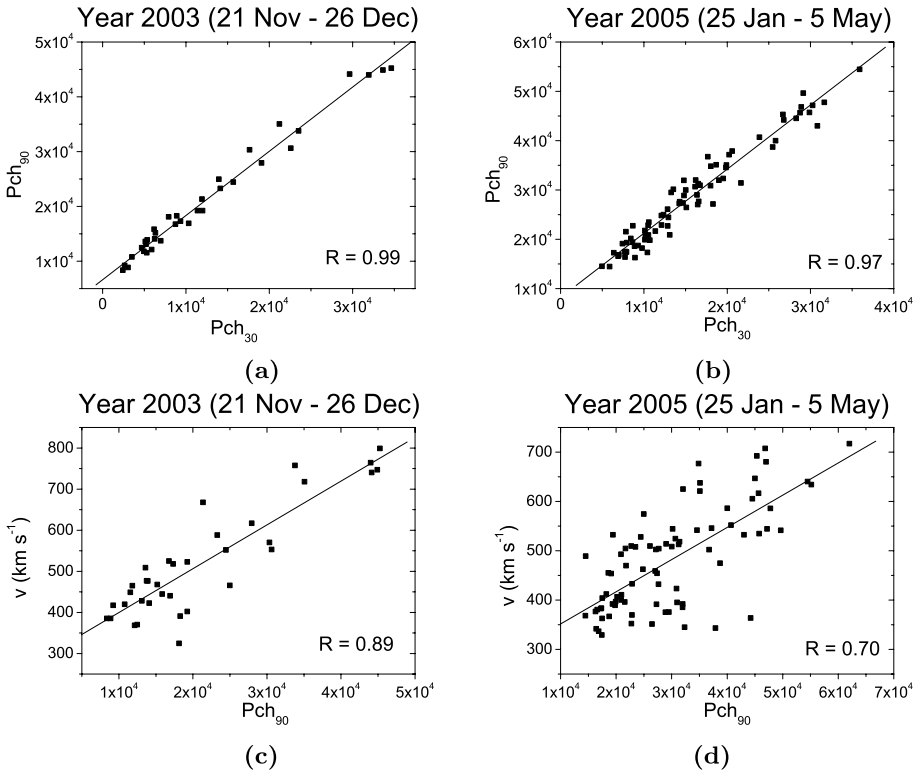
Figure 9 (a, b) Scatter plots of Pch with no restriction in the latitude range (shown as Pch$_{90}$) and former Pch results (shown as Pch$_{30}$) with the latitude domain restricted to $\pm 30°$. (c, d) Time-lagged correlations between Pch$_{90}$ and solar wind velocity v with 3-day lag. The solid lines represent linear least-squares fits to the data. The correlation coefficients of the fits (R) are indicated.

4. Summary and Conclusions

In summary, a new forecasting index Pch, which is a function of the intensity in the central ($\pm 10°$) area in SOHO EIT 284 Å images of the solar corona, has been developed to predict the daily solar wind speed 3 days in advance. The Pch factor reflects both the area and brightness effects of CHs. Our analysis showed that in periods of low CME activity the Pch factor can improve forecasting accuracy. Furthermore, removing the restriction on latitudinal range did not improve the results, which may indicate that high-latitude CHs have little influence on the CIR – high-speed stream characteristics near Earth.

Moreover, the Pch index can eliminate an important bias in the forecasting process, which is present in the methods using CH area as input parameter due to the fact that the CH boundary cannot be unambiguously determined from observations, since Pch does not depend on the CH boundary determination.

References

Borovsky, J.E., Denton, M.H.: 2006, *J. Geophys. Res.* **111**, A07S08.

Bravo, S.: 1996, *ASP Conf. Ser.* **95**, 445B.

Bravo, S., Cruz-Abeyro, J.A.L., Rojas, D.: 1998, *Ann. Geophys.* **16**, 49.

Bromage, B.J.I., Browning, P.K., Clegg, J.R.: 2001, *Space Sci. Rev.* **97**, 13.

Chertok, I.M., Mogilevsky, E.I., Obridko, V.N., Shilova, N.S., Hudson, H.S.: 2001, *Astrophys. J.* **567**, 1225.

Delaboudiniére, J.P., Artzner, G.E., Brunaud, J., Gabriel, A.H., Hochedez, J.F., Millier, F., *et al.*: 1995, *Solar Phys.* **162**, 291.

Gosling, J.T., Pizzo, V.J.: 1999, *Space Sci. Rev.* **89**, 21.

Kahler, S.W., Hudson, H.S.: 2002, *Astrophys. J.* **574**, 467.

McComas, D.J., Elliott, H.A.: 2002, *Geophys. Res. Lett.* **29**, 1314.

McComas, D.J., Bame, S.J., Barker, P., Feldman, W.C., Phillips, J.L., Riley, P., Griffee, J.W.: 1998, *Space Sci. Rev.* **86**, 563.

Persiantsev, I.G., Ryazanov, A.Yu, Shugai, Yu.S.: 2006, *Pattern Recognit. Image Anal.* **16**(1), 30.

Robbins, S., Henney, C.J., Harvey, J.W.: 2006, *Solar Phys.* **233**, 265.

Shen, C., Wang, Y., Ye, P., Wang, S.: 2006, *Astrophys. J.* **639**, 510.

Stone, E.C., Frandsen, A.M., Mewaldt, R.A., Christian, E.R., Margolies, D., Ormes, J.F., Snow, F.: 1998, *Space Sci. Rev.* **86**, 1.

Veselovsky, I.S., Persiantsev, I.G., Ryazanov, A.Yu., Shugai, Yu.S.: 2006, *Solar Syst. Res.* **40**, 427.

Vršnak, B., Temmer, M., Veronig, A.M.: 2007a, *Solar Phys.* **240**, 315.

Vršnak, B., Temmer, M., Veronig, A.M.: 2007b, *Solar Phys.* **240**, 331.

Watari, S.: 1997, *Ann. Geophys.* **15**, 662.

Zhang, J., Woch, J., Solanki, S.K., von Steiger, R.: 2002, *Geophys. Res. Lett.* **29**, 1236.

Zhang, J., Woch, J., Solanki, S.K., von Steiger, R., Forsyth, R.: 2003, *J. Geophys. Res.* **108**, 1144.

Zhao, X.P., Hoeksema, J.T., Scherrer, P.H.: 1999, *J. Geophys. Res.* **104**, 9735.